Synthesis and Transport Properties of Large-Scale Alloy $Co_{0.16}Mo_{0.84}S_2$ Bilayer Nanosheets

Bo Li,[†] Le Huang,[†] Mianzeng Zhong,[‡] Nengjie Huo,[†] Yongtao Li,[†] Shengxue Yang,[†] Chao Fan,[†] Juehan Yang,[†] Wenping Hu,[§] Zhongming Wei,[*,†,⊥] and Jingbo Li[*,†]

[†]Institute of Semiconductors, Chinese Academy of Sciences, Beijing 100083, People's Republic of China, [‡]Zhejiang Provincial Key Laboratory of Solid State Optoelectronic Devices, Zhejiang Normal University, Jinhua 321004, People's Republic of China, [§]Beijing National Laboratory for Molecular Sciences, Key Laboratory of Organic Solids, Institute of Chemistry, Chinese Academy of Sciences, Beijing 100190, People's Republic of China, and [⊥]Nano-Science Center & Department of Chemistry, University of Copenhagen, Universitetsparken 5, DK-2100 Copenhagen Ø, Denmark

ABSTRACT Synthesis of large-scale highly crystalline two-dimensional alloys is significant for revealing properties. Here, we have investigated the vapor growth process of high-quality bilayer $Co_xMo_{1-x}S_2$ (x = 0.16) hexagonal nanosheets systematically. As the initial loading of the sulfur increases, the morphology of the $Co_xMo_{1-x}S_2$ ($0 < x \leq 1$) nanosheets becomes hexagons from David stars step by step at 680 °C. We find that Co atoms mainly distribute at the edge of nanosheets. When the temperature increases from 680 to 750 °C, high-quality cubic pyrite-type crystal structure CoS_2 grows on the surface of $Co_xMo_{1-x}S_2$ nanosheet gradually and forms hexagonal film induced by the nanosheet. Electrical transport measurements reveal that the $Co_xMo_{1-x}S_2$ nanosheets and CoS_2 films exhibit n-type semiconducting transport behavior and half-metallic behavior, respectively. Theoretical calculations of their band structures agree well with the experimental results.

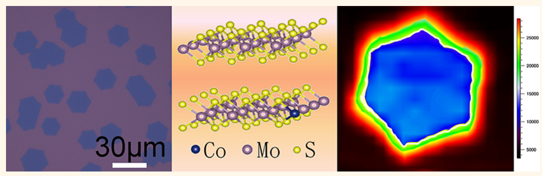

KEYWORDS: two-dimensional alloy · transition-metal dichalcogenides · $Co_xMo_{1-x}S_2$ · transport property · band structure

As more comprehensive investigations on graphene occur,[1−5] two-dimensional (2D) materials have been attracting wide interest due to their peculiar structural properties and fascinating applications in the areas of electronics, optics, biology, and catalysis.[6−12] However, the pristine graphene shows no band gap, which restricts its real application in the integrated circuit electronics. As the promising substitutes for graphene, transition-metal dichalcogenides (TMDCs) which also have layered crystalline structure with strong in-plane bonding but weak interlayer action (van der Waals force) show natural band gaps. TMDC-layered structures have unique electrical, optical, and chemical properties, and such properties obviously vary with thickness ranging from bulk to monolayer.[13−15] Since alloying in the TMDC 2D materials can realize the versatile change of their band structures, it becomes a viable method to achieve the real application of 2D materials in both electronics and optoelectronics.[16,17] Several 2D-layered TMDC alloys, such as $Mo_{1-x}W_xS_2$, $Mo_{1-x}W_xSe_2$, and $MoS_{2x}Se_{2(1-x)}$ (x = 0−1), have been synthesized recently for the study of continuous tunable optical properties.[18−22] Until now, most reports of 2D alloys TMDCs only focus on the synthesis and optical properties. Their transport property that is crucial in the device application needs further investigation. Pulickel *et al.*[22] and Xie *et al.*[23,24] reported the field-effect transport of $Mo_{1-x}W_xSe_2$ and $MoS_{2x}Se_{2(1-x)}$ alloys.

Co-doped MoS_2 (CoMoS) powder related with deep hydrodesulfurization (HDS) activity has been reported extensively.[25−28] Deepak *et al.* have confirmed that Co atoms can replace the location of Mo in MoS_2 nanowire catalysts by aberration corrected scanning transmission electron microscopy (STEM).[29] Lauritsen *et al.* have found that the Co promoter atoms are located at the edges of single-layer CoMoS nanoclusters by scanning tunneling microscopy (STM), which causes the shapes of the MoS_2 nanoclusters changing from triangular to

* Address correspondence to zmwei@semi.ac.cn, jbli@semi.ac.cn.

Received for review September 7, 2014 and accepted January 13, 2015.

Published online January 13, 2015
10.1021/nn505048y

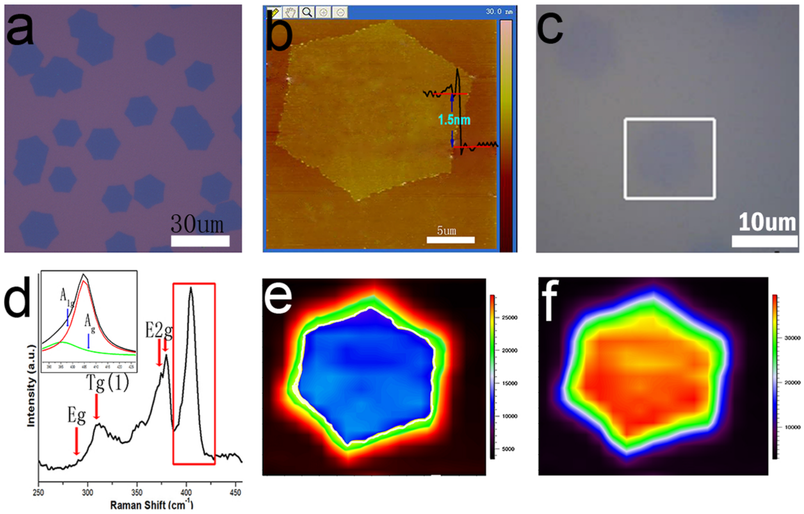

Figure 1. (a) Optical and (b) AFM images of the $Co_{0.16}Mo_{0.84}S_2$ nanosheets on the substrate, (c−f) Optical image, Raman spectrum (d) of $Co_{0.16}Mo_{0.84}S_2$ nanosheets, and corresponding Raman peak intensity mappings at 374 cm^{-1} (e) and 379 cm^{-1} (f).

hexagonally truncated.[30] As important 2D diluted magnetic semiconductors, Co-doped monolayer and bilayer MoS_2 have recently been studied by theoretical calculations.[31−34] However, the experimental realization of $Co_xMo_{1-x}S_2$ 2D layered structure has rarely been reported. Here, we have synthesized large-scale 2D alloy $Co_xMo_{1-x}S_2$ (where x can be calculated as 0.16) hexagonal bilayer nanosheets using a chemical vapor deposition (CVD) method which has achieved great success in the growth of 2D materials, such as MoS_2,[35−37] $MoSe_2$,[38−40] WS_2,[41,42] WSe_2.[43] We also reveal that the obtained hexagonal $Co_xMo_{1-x}S_2$ nanosheet can be transformed into high crystalline CoS_2 and MoS_2 film without damaging the shape through increasing the temperature. The electrical transport properties of the bilayer $Co_xMo_{1-x}S_2$ nanosheets and the CoS_2 film are also investigated both experimentally and theoretically.

RESULTS AND DISCUSSION

The hexagonal bilayer $Co_{0.16}Mo_{0.84}S_2$ nanosheet (Figure 1a) synthesized by the CVD method is characterized by Raman spectrum, atomic force microscopy (AFM), and transmission electron microscopy (TEM). The thickness of monolayer MoS_2 is about 0.7 nm,[35] and the observed height of the $Co_{0.14}Mo_{0.86}S_2$ nanosheet here is about 1.5 nm (Figure 1b), which indicates a bilayer film.

The Raman spectrum is very effective for characterizing the structures of 2D alloys, and the as-made nanosheet shows mainly six Raman peaks (Figure 1d) in the range of 250−475 cm^{-1} under 532 nm excitation assigned to CoS_2 (E_g mode ∼290 cm^{-1}, $T_g(1)$ mode ∼311 cm^{-1}, A_g mode ∼395 cm^{-1})[44] and $Co_xMo_{1-x}S_2$ alloy (A_{1g} mode ∼405 cm^{-1}, E_{2g} modes ∼379 and 374 cm^{-1}). The A_{1g} mode results from the out-of-plane vibration of only S atoms in opposite directions, and the in-plane E_{2g} modes are associated with opposite vibration of two S atoms with respect to the Mo and Co atoms (see the Supporting Information, S1). Similar to the $Mo_{1-x}W_xS_2$ alloy,[19] A_{1g} and E_{2g} modes here show one-mode and two-mode behaviors, respectively. Two phonon branches associated with E_{2g} modes of MoS_2 (379 cm^{-1}) and CoS_2 (374 cm^{-1}) are observed in the alloys. Under the same conditions, Raman peak intensity is proportional to the amount of substance. The E_{2g} peak related with CoS_2 (374 cm^{-1}) is strong at edge of the nanosheet and weak at center of the nanosheet (Figure 1e), showing that Co atoms mainly distribute at edge of the nanosheets. The E_{2g} peak related with MoS_2 (379 cm^{-1}) is strong at the center of the nanosheet but weak at the edge of the nanosheet, demonstrating that Mo atoms mainly distribute at center of the nanosheet (Figure 1f).

Transmission electron microscopy (TEM) is used to investigate the structure of the $Co_{0.16}Mo_{0.84}S_2$ nanosheet in detail (Figure 2a). The high-resolution TEM (HRTEM) images (Figure 2b, c) and the corresponding selected area electron diffraction (SAED) pattern (Figure 2d) reveal that the nanosheet has lattice spacing of 0.27 and 0.16 nm assigned to the (100) and (110) planes along the [001] zone axis, showing a high-quality hexagonal symmetry structure. The energy-dispersive X-ray spectroscopy (EDX) (Figure 2e) demonstrates that the nanosheet consists of Co, Mo, and S elements (the exhibited C and Cu elements are from the grid of copper), with the Co mole fraction [x, Co/(Co + Mo)] of ∼0.16, indicating the composition of the nanosheet is $Co_{0.16}Mo_{0.84}S_2$. X-ray photoelectron spectroscopy (XPS) is carried out to identify the composition of the nanosheet further and is similar to the TEM−EDX result (see the Supporting Information, S7).

In the growth process, we find that the equilibrium morphology of the $Co_xMo_{1-x}S_2$ nanosheets change

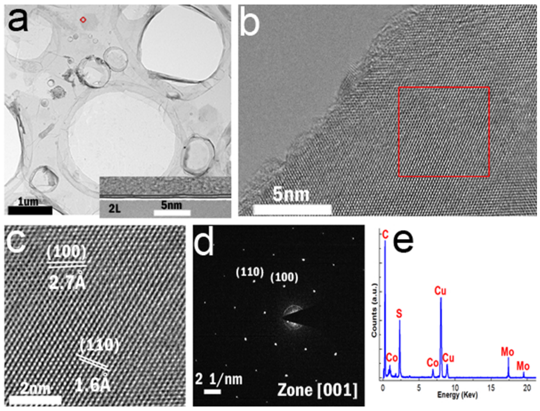

Figure 2. TEM characterizations of $Co_xMo_{1-x}S_2$ nanosheet. (a) Low-magnification TEM image of hexagonal $Co_xMo_{1-x}S_2$ nanosheet supported on holey carbon grid and a cross-section image edge (inset). (b) HRTEM image of $Co_xMo_{1-x}S_2$ nanosheet and (c) enlarged HRTEM image of the marked areas in (b). (d) SAED pattern taken on the area of the nanosheet marked in the red circle in (a). (e) Corresponding TEM–EDX profile of the sample.

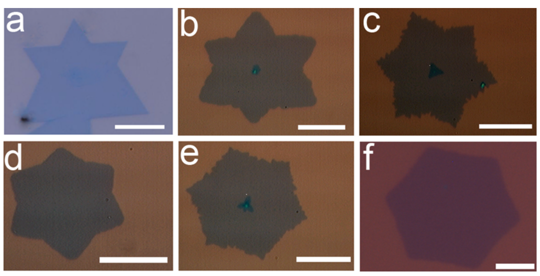

Figure 3. Effect of the initial loading of sulfur on the morphology of $Co_xMo_{1-x}S_2$ nanosheets. (a) Without Co_3O_4 in the ceramic boat. The amounts of sulfur in (b), (c), (d), (e), (f) are <0.5, 0.5–0.8, 0.8–1.2, 1.2–1.5, and 1.5–2 g, respectively. The scale bars are 10 μm.

into hexagons from Star of David shapes[45] gradually with increasing the initial loading of the sulfur at relatively low temperature (680 °C) (Figure 3). Grain boundaries are important in 2D materials and have been widely investigated.[46–48] Grain boundaries emerge at the edge of the Star of David shape, while the center area of the star shows high crystallinity (see the Supporting Information, S6). We have calculated the total energy of of the Star of David and hexagonal $Co_xMo_{1-x}S_2$ nanosheet by density functional theory (DFT), and the results show that Co doped at edge sites is more stable than that at center sites (see Supporting Information, S2). Krebs *et al.* have investigated the morphology and edges of the CoMoS nanocrystallites related with different chemical potential of S ($\Delta\mu_s$) in the gas phase by DFT calculations.[49] $\Delta\mu_s$ depends on the partial pressures of H_2S and H_2; the temperature also affects the affinity of Co promoter for the S edge and Mo edge. Under high $\Delta\mu_s$, Co exhibits a similar affinity on both edges, which tends to stabilize the Co promoter and form regular shapes. On the contrary, the decrease of $\Delta\mu_s$ enhances the affinity of Co for the S edge compared with that for the Mo edge, which leads to irregular morphology of the CoMoS nanocrystallites with asymmetrical edges. In our experiments, instead of H_2S, we use sulfur powder which is more preferable because of its accessibility and safety. The partial pressure of sulfur stream rises when the initial loading of the sulfur is increased at a certain temperature, which leads to higher $\Delta\mu_s$. Thus, the $\Delta\mu_s$ is in direct proportion to the initial loading of the sulfur. In the case of an insufficient sulfur supply and low $\Delta\mu_s$, Co promoters are more favorable to be located at the S edge than at the Mo edge for lower edge energy. As a result, the selectivity of Co promoters results in the irregularity of the local morphology. As the sulfur supply and $\Delta\mu_s$ rise, Co promoters exhibit an almost similar affinity for both edges and are well distributed. At high concentration of sulfur steam, the growth of $Co_xMo_{1-x}S_2$ nanosheets is more sufficient with regular morphology and less dangling bonds at the edges.

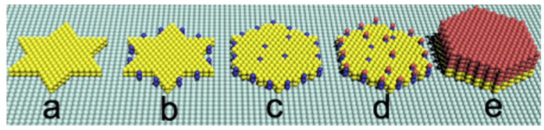

Figure 4. Stimulated models of growth process vary with sulfur concentration and temperatures. Yellow spheres represent MoS_2; purple and red spheres stand for Co promoters and CoS_2, respectively.

In the growth process of such alloy bilayers, another important parameter interrelated to the sulfur concentration is temperature. When the temperature rises to 750 °C, a bilayer structure with upper CoS_2 and bottom MoS_2 films (CoS_2–MoS_2 film) (see the Supporting Information, S3) is obtained. The growth process of $Co_xMo_{1-x}S_2$ nanosheet and CoS_2–MoS_2 film varies with the sulfur concentration and temperature. With the temperature increasing from room temperature to 680 °C, MoO_3 nucleates forms on the substrate first by the easier evaporation with respect to Co_3O_4 and then grows into bilayer MoS_2 (Figure 4a). Co_3O_4 reacts with S to provide Co promoters at the edges of the nanosheet (Figure 4b). Under an adequate supply of S, the edges of the nanosheet become zigzag motifs and expand to hexagon gradually with the reaction of Co, Mo, and S (Figure 4c). It is noted that the Co promoters are not only at the edges but also in the middle of the nanosheet when it turns into large-scale hexagon. On the surface of the nanosheets there also exist CoS_2 nanoparticles which may be produced by the growth of nucleus from the Co promoters in the nanosheet (Figure 4d). The edges of the nanosheet where plenty of CoS_2 particles aggregated become thicker when the temperature increases from 680 to 750 °C, and then a large-scale high-quality hexagonal CoS_2 film eventually appears on the surface (Figure 4e).

Although 2D alloys have been synthesized in different ways,[16–21,23,50] their transport measurements of

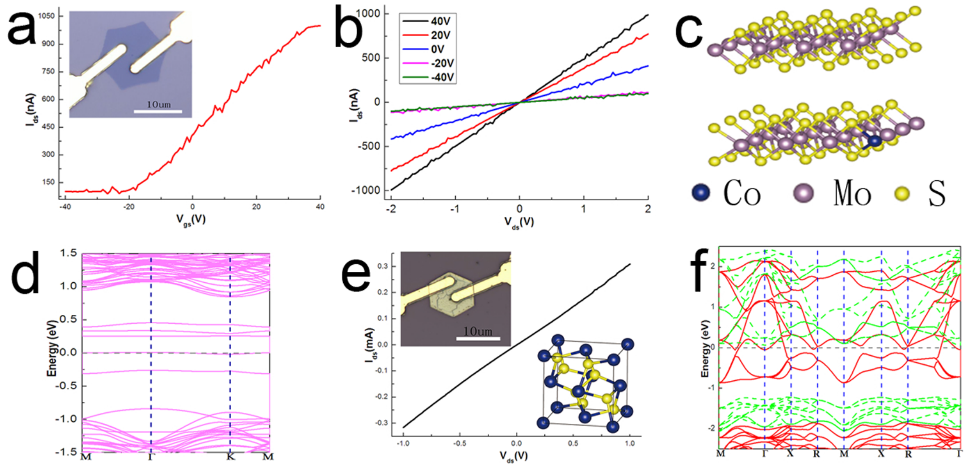

Figure 5. Electrical transport properties of $Co_xMo_{1-x}S_2$ nanosheet and CoS_2 film. (a) Room-temperature characteristics of the $Co_xMo_{1-x}S_2$ nanosheet FET devices with 2 V applied bias voltage. The inset shows the optical image of a FET device. (b) Drain current−voltage curves acquired at varied V_{gs} from −40 to +40 V representing a good ohmic contact. (c) Atomic structure of the calculated $Co_xMo_{1-x}S_2$ bilayer. Blue, purple, and yellow balls denote Co, Mo, and S atoms, respectively. (d) Corresponding band structure of the bilayer. The horizontal line dashed lines indicate the Fermi level. (e) *I*−*V* curve for the CoS_2 film at room-temperature. The insets show the crystal structure of CoS_2 (blue and yellow spheres stand for Co and S atoms, respectively) and optical image of a FET device. I_{ds} and V_{ds} are drain-to-source current and voltage, respectively. (f) Band structure calculated from DFT for bulk CoS_2. The horizontal line dashed lines indicate the Fermi level.

field-effect transistor (FET) devices have rarely been reported.[22−24] To evaluate the electrical performance of the $Co_xMo_{1-x}S_2$ nanosheet, we fabricate FETs through the lithography process with 3 μm channel length on a $Co_xMo_{1-x}S_2$ nanosheet using 5 nm Cr/50 nm Au as source and drain electrodes, 300 nm thick SiO_2 as dielectrics, and n^{++} Si as the back gate. We find that $Co_xMo_{1-x}S_2$ nanosheet devices demonstrated FET characteristics of a n-type semiconductor (Figure 5a and b), with a mobility as high as 0.52 $cm^2/(V\ s)$ (see the Supporting Information, S9), the on/off ratio (about 10) (Figure 5a) is lower than the reported bilayer MoS_2 flakes.[51−53] In order to further understand the electronic properties of the $Co_xMo_{1-x}S_2$ bilayer, we constructed a $Co_xMo_{1-x}S_2$ supercell containing 31 Mo, 64 S, and 1 Co atoms by the generalized gradient approximation (GGA) for the exchange-correlation functional (Figure 5c). Figure 6 shows the schematic plot of a $Co_xMo_{1-x}S_2$ nanosheet transistor on the on state (Figure 6b) and off state (Figure 6c). The results show that deep-impurity levels emerge around the Fermi energy of the nanosheet (Figure 5d), and the low on/off ratio should result from the deep-impurity levels where carriers (electrons) accumulate when the back gate voltage (V_{gs}) is negative (off state) (Figure 6c). On the other hand, as some impurity levels exist in the nanosheets, conduction band will obtain more free electrons by thermal excitation at room temperature, compared with pure MoS_2. Both of the two situations will lead to the relatively large off state current. Additionally, defects (such as vacancy, dislocation) and small half-metallic CoS_2 nanoparticles on the surface of the nanosheet diminish regulating carrier concentration by gate voltage.

The I−V curve of CoS_2 film (Figure 5e) recorded under ambient conditions shows the ohmic response and half-metallic behavior with a high conductivity about 8×10^4 s/m (see the Supporting Information, S8). Band structure of CoS_2 has been calculated using the (GGA) for the exchange-correlation functional (Figure 5f). Band dispersion for the spin-up state and spin-down state are plotted by red and green lines, respectively. There is no spin-down state at Fermi level and CoS_2 is clearly half-metallic,[54−56] agreeing well with our experimental results.

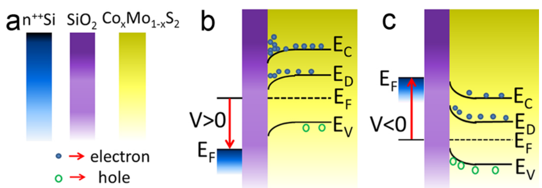

Figure 6. (a) Schematic plot of the $Co_xMo_{1-x}S_2$ nanosheet transistor. (b, c) Band diagram under positive and negative V_{gs}, respectively. *V*, E_F, E_C, E_D, and E_V represent back gate voltage, the Fermi level, conduction band level, impurity level, and valence band level, respectively.

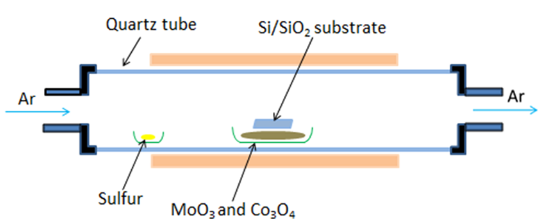

Figure 7. Configuration used in our experiments for $Co_xMo_{1-x}S_2$ nanosheet and CoS_2−MoS_2 film preparation.

CONCLUSION

In summary, we have successfully synthesized large-scale hexagonal bilayer $Co_{0.16}Mo_{0.84}S_2$ nanosheets and it is found that the morphology of the nanosheets varies with the initial loading of sulfur and temperature. The A_{1g} mode and E_{2g} modes show one-mode and two-mode behaviors, respectively. We have also illuminated that CoS_2 film can form on top of the hexagonal nanosheets under high temperature. The template induced method obtaining CoS_2 film provides a new direction in controlling 2D material shapes. Field effect transistor based on the bilayer $Co_xMo_{1-x}S_2$ nanosheet shows a typical n-type transport behavior. CoS_2 film exhibits a half-metallic behavior with the conductivity about 8×10^4 s/m. Such transport properties also agree well with the calculation for their band structures. These alloy nanosheets of $Co_xMo_{1-x}S_2$ should have large potential applications in the tunable optoelectronics.

EXPERIMENTAL SECTION

A ceramic boat containing mixed MoO_3 (3 mg) and Co_3O_4 (300 mg) powder was placed in the center of a tube furnace, and bare Si/SiO_2 substrates were placed on top of the powders. Another ceramic boat holding pure sulfur (S) was placed at the upwind low temperature zone in the quartz tube. During the reaction, the temperature of the low temperature zone was controlled to be a little above the melting point of S (113 °C). The quartz tube was first kept in a flowing protective atmosphere of high purity Ar (99.9999%) with the flow rate of 150−200 sccm. After 30 min of Ar purging, the furnace temperature was gradually increased from room temperature to 680 °C/750 °C in 25 min. Then the temperature was kept at 680 °C/750 °C for 5 min. Figure 7 shows a schematic illustration of the reaction condition of this CVD process.

Conflict of Interest: The authors declare no competing financial interest.

Acknowledgment. This work was supported by the National Natural Science Foundation of China under Grant No. 91233120 and the National Basic Research Program of China (2011CB921901).

Supporting Information Available: Composition-dependent A'_1 mode and E' mode frequencies in $Co_xMo_{1-x}S_2$ monolayer using MREI model, analysis of more stable doping sites in bilayer $Co_xMo_{1-x}S_2$ nanosheet by first-principles calculations, effect of temperature on the growth processes, TEM images of $Co_xMo_{1-x}S_2$ synthesized at 700 °C, Raman spectrum and AFM image of the CoS_2-MoS_2 film, TEM characterizations of $Co_xMo_{1-x}S_2$ David star, XPS spectra of $Co_xMo_{1-x}S_2$ nanosheets, calculations of CoS_2 conductivity, and field-effect mobility of $Co_xMo_{1-x}S_2$ nanosheet. This material is available free of charge *via* the Internet at http://pubs.acs.org.

REFERENCES AND NOTES

1. Novoselov, K. S.; Geim, A. K.; Morozov, S.; Jiang, D.; Zhang, Y.; Dubonos, S.; Grigorieva, I.; Firsov, A. Electric Field Effect in Atomically Thin Carbon Films. *Science* **2004**, *306*, 666–669.
2. Xiao, H.; Zongyou, Y.; Shixin, W.; Q, X.; H, Q.; Z, Q.; Qingyu, Y.; Freddy, B.; Zhang, H. Graphene-Based Materials: Synthesis, Characterization, Properties, and Applications. *Small* **2011**, *7*, 1876–1902.
3. Xiao, H.; Q, X.; Freddy, B.; Zhang, H. Graphene-Based Composites. *Chem. Soc. Rev.* **2012**, *41*, 666–686.
4. Zheng, L.; Lulu, M.; Gang, S.; Wu, Z.; Yongji, G.; Sidong, L.; Xuebei, Y.; Jiangnan, Z.; Jingjiang, Y.; Ken, P. H.; et al. In-Plane Heterostructures of Graphene and Hexagonal Boron Nitride with Controlled Domain Sizes. *Nat. Nanotechnol.* **2013**, *8*, 119–124.
5. Yongji, G.; Gang, S.; Zhuhua, Z.; Wu, Z.; Jeil, J.; Weilu, G.; Lulu, M.; Yang, Y.; Shubin, Y.; Ge, Y.; et al. Direct Chemical Conversion of Graphene to Boronand Nitrogen- and Carbon-Containing Atomic Layers. *Nat. Commun.* **2014**, *5*, 3193.
6. Lightcap, I. V.; Kosel, T. H.; Kamat, P. V. Anchoring Semiconductor and Metal Nanoparticles on A Two-Dimensional Catalyst Mat. Storing and Shuttling Electrons with Reduced Graphene Oxide. *Nano Lett.* **2010**, *10*, 577–583.
7. Xiehong, C.; Zongyou, Y.; Zhang, H. Three-Dimensional Graphene Materials: Preparation, Structures and Application in Supercapacitors. *Energy Environ. Sci.* **2014**, *7*, 1850–1865.
8. Zongyou, Y.; Jixin, Z.; Qiyuan, H.; Xiehong, C.; Chaoliang, T.; Hongyu, C.; Qingyu, Y.; Zhang, H. Graphene-Based Materials for Solar Cell Applications. *Adv. Energy Mater.* **2014**, *4*, 1300574.
9. Xiao, H.; Zhiyuan, Z.; Zhang, H. Metal Dichalcogenide Nanosheets: Preparation, Properties and Applications. *Chem. Soc. Rev.* **2013**, *42*, 1934–1946.
10. Hai, L.; Jumiati, W.; Zongyou, Y.; Zhang, H. Preparation and Applications of Mechanically Exfoliated Single-Layer and Multilayer MoS_2 and WSe_2 Nanosheets. *Acc. Chem. Res.* **2014**, *47*, 1067–1075.
11. Xiao, H.; Chaoliang, T.; Zongyou, Y.; Zhang, H. Hybrid Nanostructures Based on Two-Dimensional Nanomaterials. *Adv. Mater.* **2014**, *26*, 2185–2204.
12. Yongji, G.; Junhao, L.; Xingli, W.; Gang, S.; Sidong, L.; Zhong, L.; Xiaolong, Z.; Gonglan, Y.; Robert, V.; Boris, I. Y. Vertical and In-Plane Heterostructures from WS_2/MoS_2 Monolayers. *Nat. Mater.* **2014**, *13*, 1135–1142.
13. Radisavljevic, B.; Radenovic, A.; Brivio, J.; Giacometti, V.; Kis, A. Single-Layer MoS_2 Transistors. *Nat. Nanotechnol.* **2011**, *6*, 147–150.
14. Tsai, D. S.; Liu, K. K.; Lien, D. H.; Tsai, M. L.; Kang, C. F.; Lin, C. A.; Li, L. J.; He, J. H. Few-Layer MoS_2 with High Broadband Photogain and Fast Optical Switching for Use in Harsh Environments. *ACS Nano* **2013**, *7*, 3905–3911.
15. Gutiérrez, H. R.; Perea-López, N.; Elas, A. L.; Berkdemir, A.; Wang, B.; Lv, R.; López-Uras, F.; Crespi, V. H.; Terrones, H.; Terrones, M. Extraordinary Room-Temperature Photoluminescence in Triangular WS_2 Monolayers. *Nano Lett.* **2012**, *13*, 3447–3454.
16. Dumcenco, D. O.; Su, Y. C.; Wang, Y. P.; Chen, K. Y.; Huang, Y. S.; Ho, C. H.; Tiong, K. K. Polarization Dependent Raman Active Modes Study of the $Mo_{1-x}W_xS_2$ Mixed Layered Crystals. *Chin. J. Phys.* **2011**, *49*, 270–277.
17. Chen, Y.; Xi, J.; Dumcenco, D. O.; Liu, Z.; Suenaga, K.; Wang, D.; Shuai, Z.; Huang, Y.-S.; Xie, L. Tunable Band Gap Photoluminescence from Atomically Thin Transition-Metal Dichalcogenide Alloys. *ACS Nano* **2013**, *7*, 4610–4616.
18. Liu, H.; Antwi, K. A.; Chua, S.; Chi, D. Vapor-Phase Growth and Characterization of $Mo_{1-x}W_xS_2$ Atomic Layers on 2-in. Sapphire Substrates. *Nanoscale* **2014**, *6*, 624–629.
19. Chen, Y.; Dumcenco, D. O.; Zhu, Y.; Zhang, X.; Mao, N.; Feng, Q.; Zhang, M.; Zhang, J.; Tan, P.-H.; Huang, Y.-S.; et al. Composition-Dependent Raman Modes of $Mo_{1-x}W_xS_2$ Monolayer Alloys. *Nanoscale* **2014**, *6*, 2833–2839.
20. Li, H.; Duan, X.; Wu, X.; Zhuang, X.; Zhou, H.; Zhang, Q.; Zhu, X.; Hu, W.; Ren, P.; Guo, P.; et al. Growth of Alloy $MoS_{2x}Se_{2(1-x)}$ Nanosheets with Fully Tunable Chemical Compositions and Optical Properties. *J. Am. Chem. Soc.* **2014**, *136*, 3756–3759.
21. Su, S. H.; Hsu, W. T.; Hsu, C. L.; Chen, C. H.; Chiu, M. H.; Lin, Y. C.; Chang, W. H.; Suenaga, K.; He, H., Jr; Li, L. J. Controllable Synthesis of Band-Gap-Tunable and Monolayer Transition-Metal Dichalcogenide Alloys. *Nanoenergy Technol. Mater.* **2014**, *2*, 27.

22. YJ, G.; Zheng, L.; L, A. R.; Gang, S.; Sina, N.; Zhong, L.; Ana, E. L.; Ayse, B.; Ge, Y.; Humberto, T.; et al. Band Gap Engineering and Layer-by-Layer Mapping of Selenium-Doped Molybdenum Disulfide. *Nano Lett.* **2014**, *14*, 442–449.
23. Zhang, M.; Wu, J.; Zhu, Y.; Dumcenco, D. O.; Hong, J.; Mao, N.; Deng, S.; Chen, Y.; Yang, Y.; Jin, C.; et al. Two-Dimensional Molybdenum Tungsten Diselenide Alloys: Photoluminescence, Raman Scattering, and Electrical Transport. *ACS Nano* **2014**, *8*, 7130–7137.
24. Qingliang, F.; Zhu, Y.; Hong, J.; Zhang, M.; Duan, W.; Mao, N.; Wu, J.; Xu, H.; Ddong, F.; Lin, F.; et al. Growth of Large Area 2D $MoS_{2(1-x)}Se_{2x}$ Semiconductor Alloys. *Adv. Mater.* **2014**, *26*, 2648–2653.
25. Whitehurst, D. D.; Isoda, T.; Mochida, I. Present State of the Art and Future Challenges in the Hydrodesulfurization of Polyaromatic Sulfur Compounds. *Adv. Catal.* **1998**, *42*, 345–471.
26. Bouwens, S.; Van Veen, J.; Koningsberger, D.; De Beer, V.; Prins, R. Extended X-Ray Absorption Fine Structure Determination of the Structure of Cobalt in Carbonsupported Co and Co-Mo Sulfide Hydrodesulfurization Catalysts. *J. Phys, Chem.* **1991**, *95*, 123–134.
27. Topse, H.; Clausen, B. S. Importance of Co-Mo-S Type Structures in Hydrodesulfurization. *Catal. Rev. Sci. Eng.* **1984**, *26*, 395–420.
28. Wang, S.; An, C.; He, J.; Wang, Z.; Yuan, J. Composite Surfactants Aided Solvothermal Synthesis and Catalytic Hydrogenation Property of Oil Soluble Bimetallic CoMoS Nanoparticles. *J. Nat. Gas Chem.* **2010**, *19*, 397–402.
29. Deepak, F. L.; Esparza, R.; Borges, B.; Lopez-Lozano, X.; Jose-Yacaman, M. Direct Imaging and Identification of Individual Dopant Atoms in MoS_2 and WS_2 Catalysts by Aberration Corrected Scanning Transmission Electron Microscopy. *ACS Catal.* **2011**, *1*, 537–543.
30. Lauritsen, J.; Helveg, S.; Lægsgaard, E.; Stensgaard, I.; Clausen, B.; Topsøe, H.; Besenbacher, F. Atomic-Scale Structure of Co-Mo-S Nanoclusters in Hydrotreating Catalysts. *J. Catal.* **2001**, *197*, 1–5.
31. Cheng, Y.; Zhu, Z.; Mi, W.; Guo, Z.; Schwingenschlögl, U. Prediction of Two-Dimensional Diluted Magnetic Semiconductors: Doped Monolayer MoS_2 Systems. *Phys. Rev. B* **2013**, *87*, 100401.
32. Yue, Q.; Chang, S.; Qin, S.; Li, J. Functionalization of Monolayer MoS_2 by Substitutional Doping: A First-Principles Study. *Phys. Lett. A* **2013**, *377*, 1362–1367.
33. Huang, Z.; Peng, X.; Yang, H.; He, C.; Xue, L.; Hao, G.; Zhang, C.; Liu, W.; Qi, X.; Zhong, J. The Structural, Electronic and Magnetic Properties of Bi-Layered MoS_2 with Transition-Metals Doped in the Interlayer. *RSC Adv.* **2013**, *3*, 12939–12944.
34. Mishra, R.; Zhou, W.; Pennycook, S. J.; Pantelides, S. T.; Idrobo, J.-C. Long-Range Ferromagnetic Ordering in Manganese-Doped Two-Dimensional Dichalcogenides. *Phys. Rev. B* **2013**, *88*, 144409.
35. Lee, Y. H.; Zhang, X. Q.; Zhang, W.; Chang, M. T.; Lin, C. T.; Chang, K. D.; Yu, Y. C.; Wang, J. T.W.; Chang, C. S.; Li, L. J.; et al. Synthesis of Large-Area MoS_2 Atomic Layers with Chemical Vapor Deposition. *Adv. Mater.* **2012**, *24*, 2320–2325.
36. Zhang, W.; Huang, J. K.; Chen, C. H.; Chang, Y. H.; Cheng, Y. J.; Li, L. J. High-Gain Phototransistors Based on a CVD MoS_2 Monolayer. *Adv. Mater.* **2013**, *25*, 3456–3461.
37. Li, B.; Yang, S.; Huo, N.; Li, Y.; Yang, J.; Li, R.; Fan, C.; Lu, F. Growth of Large Area Few-Layer or Monolayer MoS_2 from Controllable MoO_3 Nanowires Nucleus. *RSC Adv.* **2014**, *4*, 26407–26412.
38. Xia, J.; Huang, X.; Liu, L.; Wang, M.; Wang, L.; Huang, B.; Zhu, D.; Li, J. J.; Gu, C. Z.; Meng, X. CVD Synthesis of Large-Area Highly Crystalline $MoSe_2$ Atomic Layers on Diverse Substrates and Photodetector Application. *Nanoscale* **2014**, *6*, 8949–8955.
39. Wang, X.; Gong, Y.; Shi, G.; Chow, W. L.; Keyshar, K.; Ye, G.; Vajtai, R.; Lou, J.; Liu, Z.; Ringe, E.; et al. Chemical Vapor Deposition Growth of Crystalline Monolayer $MoSe_2$. *ACS Nano* **2014**, *8*, 5125–5131.
40. Shaw, J. C.; Zhou, H.; Chen, Y.; Weiss, N. O.; Liu, Y.; Huang, Y.; Duan, X. Chemical Vapor Deposition Growth of Monolayer $MoSe_2$ Nanosheets. *Nano Res.* **2014**, *7*, 1–7.
41. Cong, C.; Shang, J.; Wu, X.; Cao, B.; Peimyoo, N.; Qiu, C.; Sun, L.; Yu, T. Synthesis and Optical Properties of Large-Area Single-Crystalline 2D Semiconductor WS_2 Monolayer from Chemical Vapor Deposition. *Adv. Opt. Mater.* **2014**, *2*, 131–136.
42. Tongay, S.; Fan, W.; Kang, J.; Park, J.; Koldemir, U.; Suh, J.; Narang, D.; Liu, K.; Ji, J.; Li, J.; et al. Tuning Interlayer Coupling in Large-Area Heterostructures with CVD-Grown MoS_2 and WS_2 Monolayers. *Nano Lett.* **2014**, *14*, 3185–3190.
43. Huang, J. K.; Pu, J.; Hsu, C. L.; Chiu, M. H.; Juang, Z. Y.; Chang, Y. H.; Chang, W. H.; Iwasa, Y.; Takenobu, T.; Li, L. J. Large-Area Synthesis of Highly Crystalline WSe_2 Monolayers and Device Applications. *ACS Nano* **2014**, *8*, 923–930.
44. Lyapin, S.; Utyuzh, A.; Petrova, A.; Novikov, A.; Lograsso, T.; Stishov, S. Raman Studies of Nearly Half-Metallic Ferromagnet CoS_2. *arXiv preprint arXiv:1402.5785*, **2014**.
45. Zhong, L.; T, M. T.; Ana, L. E.; Simin, F.; Chanjing, Z.; Kazunori, F.; Fujisawa, N. P.; Victor, C.; Humberto, T.; Mauricio, T. Facile Synthesis of MoS2 and $Mo_xW_{1-x}S_2$ Triangular Monolayers. *Appl. Phys. Lett. Mater.* **2014**, *2*, 092514.
46. Pulickel, M. A.; Y, B. I. Graphene: Pushing the Boundaries. *Nat. Mater.* **2011**, *10*, 415–417.
47. Idrobo, J. C.; Ajayan, P. M.; Lou, J. Vapour Phase Growth and Grain Boundary Structure of Molybdenum Disulphide Atomic Layers. *Nat. Mater.* **2013**, *12*, 754–759.
48. Zande, A. M.; Huang, P. Y.; Chenet, D. A.; Berjekbacg, T. C.; You, Y.; Lee, G.-H.; Heinz, T. F.; Reichman, D. R.; Muller, D. A.; Hone, J. C. Grains and Grain Boundaries in Highly Crystalline Monolayer Molybdenum Disulphide. *Nat. Mater.* **2013**, *12*, 554–561.
49. Krebs, E.; Daudin, A.; Raybaud, P. A DFT Study of CoMoS and NiMoS Catalysts: from Nano-Crystallite Morphology to Selective Hydrodesulfurization. *Oil Gas Sci. Technol.* **2009**, *64*, 707–718.
50. Dumcenco, D. O.; Kobayashi, H.; Liu, Z.; Huang, Y.-S.; Suenaga, K. Visualization and Quantification of Transition Metal Atomic Mixing in $Mo_{1-x}W_xS_2$ Single Layers. *Nat. Comm* **2013**, *4*, 1351.
51. Wang, H.; Yu, L.; Lee, Y. H.; Shi, Y.; Hsu, A.; Chin, M. L.; Li, L. J.; Dubey, M.; Kong, J.; Palacios, T. Integrated Circuits Based on Bilayer MoS_2 Transistors. *Nano Lett.* **2012**, *12*, 4674–4680.
52. Wu, W.; De, D.; Chang, S.-C.; Wang, Y.; Peng, H.; Bao, J.; Pei, S.-S. High Mobility and High On/Off Ratio Field-Effect Transistors Based on Chemical Vapor Deposited Single-Crystal MoS_2 grains. *Appl. Phys. Lett.* **2013**, *102*, 142106.
53. Das, S.; Chen, H.-Y.; Penumatcha, A. V.; Appenzeller, J. High Performance Multilayer MoS_2 Transistors with Scandium Contacts. *Nano Lett.* **2012**, *13*, 100–105.
54. Zhao, G.; Callaway, J.; Hayashibara, M. Electronic Structures of Iron and Cobalt Pyrites. *Phys. Rev. B* **1993**, *48*, 15781.
55. Kwon, S.; Youn, S.; Min, B. Itinerant Ferromagnetism in Half-Metallic CoS_2. *Phys. Rev. B* **2000**, *62*, 357.
56. Wang, L.; Chen, T.; Leighton, C. Spin-Dependent Band Structure Effects and Measurement of the Spin Polarization in the Candidate Half-Metal CoS_2. *Phys. Rev. B* **2004**, *69*, 094412.